Revealing the interplay between the structural complexity of triphenylamine redox derivatives and their charge transport processes via computational modeling

ARTICLE

Revealing the interplay between the structural complexity of triphenylamine redox derivatives and their charge transport processes via computational modeling

Robert Herzhoff,[a] Fabrizia Negri,[b] Klaus Meerholz,[a*] Daniele Fazzi [b*]

Triphenylamine derivatives (**TPA**s) are organic functional materials well known for their semiconducting charge transport and redox properties. Such features characterize their applications in the field of organic electronics, for instance as hole transport layer for organic light emitting diodes (OLEDs), and perovskite-based solar cells (PSCs), as well as organic cathodes for electrochemical energy storage (EES) devices (e.g. organic batteries). Despite a large number of experimental and computational investigations, some structure-property relationships remain still elusive. Here, we explore through a bottom-up computational approach the molecular and solid state structures, as well as the charge transport processes in amorphous and single crystalline phases of four different redox active **TPA**s, characterized by increased molecular structure complexity. The **TPA**s here considered feature one-, two- or four-redox centers, namely i) a single **TPA** unit, two **TPA**s linked via ii) a flexible diphenyl bridge (**TPD**) or iii) a rigid fluorene bridge (**FTPD**), and iv) four **TPA**s connected via a spiro-center (***spiro*-OMeTAD**). A combination of density functional theory, semiempirical and molecular dynamics methods is used to analyse the experimental crystalline structures, to generate the amorphous morphologies, and to calculate the charge transport parameters and hole mobility. Our results show that short- and long-range structural order in condensed phases are strongly influenced by the molecular architecture. Furthermore, charge transport parameters, such as site energies, reorganization energies and coupling integrals, are intimately coupled with the number of redox centers and the way they are connected. The charge transport is differently characterized depending on the degree of morphological disorder, namely reorganization energy-controlled transport in the crystalline phase and site-energy static-disorder controlled transport in the amorphous phase. The computed hole bulk mobilities for both single crystal and amorphous cases are in good agreement with the available experimental literature data.

Introduction

Triphenylamines (**TPA**s) are commonly used in various (opto-)electronic devices due to their good hole-transporting properties [1–4], their high redox potential vs. Li/Li^+ and cycling stability [5], and their high glass transition temperature.[6,7] Moreover, they are readily synthetically available, allowing for fine-tuning of their redox, spectroscopic and charge transport properties through the use of electro-active substituents. [8,9] **TPA**s are used as Hole Transporting Layers (HTL) in Organic Light Emitting Diodes (OLEDs) [4,10], Organic Solar Cells (OSC) [11], Perovskite Solar Cells (PSCs) [12], and also as redox-active materials for rechargeable Electrochemical Energy Storage (EES) applications, such as organic batteries and supercapacitors. [9,13] Due to the popularity of such compounds in organic electronics (especially OLED applications), a significant number of experimental publications [12,14–16], as well as theoretical and computational investigations, have been reported. [17–22] Fundamental charge transport parameters, such as the inner reorganization energy (λ_{int}), have been studied systematically at multiple levels of theory and relevant structural parameters have been identified. [20,23,24] Charge mobilities for various triphenylamine derivatives have been computed in the amorphous phase in good agreement with experimental data. [17] However, some questions concerning the relationships between the molecular structure, bulk morphology, and charge transport properties still remain to be answered. For example, it is not clear how the presence of one-, two- or more redox centers (i.e., triphenylamine units) affects the supramolecular organisation in the solid state, for both crystalline and amorphous phases, and how it impacts on the charge transport parameters and the charge mobility, specifically with respect to the mixed-valence nature of the multi-**TPA** compounds. Herein, we analyse such aspects as well as the influence of crystal packing and amorphous morphologies on the degree of charge transport isotropy/anisotropy. These issues have not been comprehensively addressed so far, in particular a systematic comparison between the computed charge transport parameters and hole mobilities in single crystalline vs. amorphous morphologies.

We focus on a library of four triphenylamine derivatives showing increasing molecular structure complexity, namely triphenylamine (**TPA**), N,N′-Bis-(3-methylphenyl)-N,N′-diphenylbenzidin (**TPD**), N^2,N^2,N^7,N^7-Tetrakis(4-methoxyphenyl)-9,9-dimethyl-9*H*-fluorene-2,7-diamine (**FTPD**), and N^2,N^2,$N^{2\prime}$,$N^{2\prime}$,N^7,N^7,$N^{7\prime}$,$N^{7\prime}$Octakis(4-methoxyphenyl)-9,9′-spirobi[fluorene]-2,2′,7,7′-tetraamine (***spiro*-OMeTAD**) (see Figure 1). Ideally, we would have chosen identical substitution patterns for all cases (i.e. para-methoxy substituents on the peripheral aryl substituents, such as MeO-**TPD**), however, we were limited to the compounds for which experimental crystal structures are available in the literature. While **TPA** has one redox center, **TPD** and **FTPD** have two redox centers, as connected either via a flexible bridge (**TPD**) or by a rigid (ladder type) one (**FTPD**), and finally ***spiro*-OMeTAD** has four redox centers, consisting of two **FTPD**-subunits that are orthogonally connected via a central spiro carbon. Such increasing structural complexity impacts the inter-molecular packing and morphological properties, as well as the charge transport processes in the bulk phase. The goal of our work is to rationalize via a bottom-up molecular modeling approach the impact of different molecular structures, as characterized by various internal torsional degrees of freedom and steric demand, on both the morphological and charge-transport properties for both crystalline and amorphous states. To this end, a computational methodology was chosen, that focuses on accurately describing the energetic and static disorder as well as those charge transport parameters intimately connected to the molecular structure.

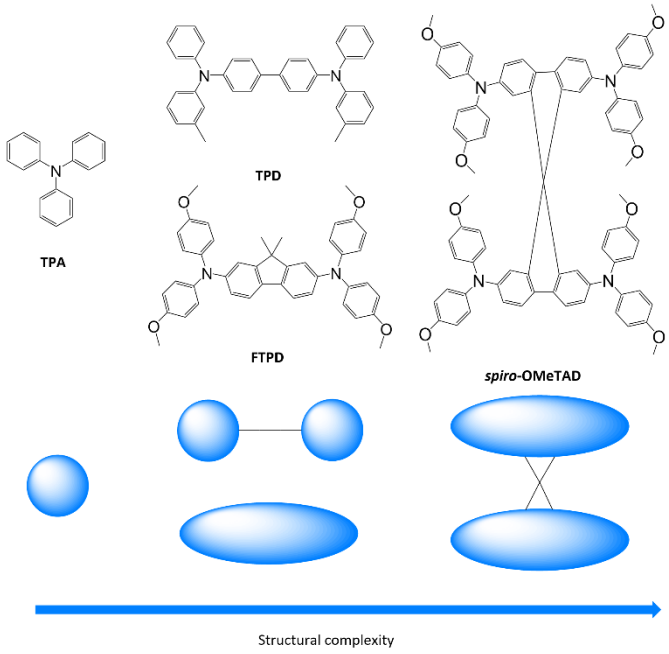

Figure 1: Triphenylamine derivatives investigated in this work (**TPA**, **TPD**, **FTPD** and ***spiro*-OMeTAD**) with simplified sketches showing their structural complexity.

By combining density functional theory (DFT), molecular dynamics (MD), and kinetic Monte-Carlo (KMC) methods we simulated the molecular and bulk properties, encompassing the calculation of the charge transport parameters and charge mobility. For each species, we analysed both single crystalline (experimental (XRD)) and amorphous phases (generated via MD simulations), focusing on the impact of the structural complexity as well as the morphological and static energetic disorder on the charge transport properties. We found a subtle interplay between the molecular structure complexity (namely one-, two- and four redox centers differently linked), supramolecular organizations, and charge transport mechanisms. The molecular geometry and shape impacts not only the supramolecular organization in the condensed phases but also the reorganization energy and the isotropy of charge carrier diffusion via its short- and long-range effect on the crystal packing, as well as the site energy difference distributions in the amorphous phase.

Computational methods

Single molecule equilibrium geometries

The calculations were performed at multiple computational levels. For the DFT calculations, the range separated hybrid functional with Grimme's scheme of dispersion corrections ωB97X-D [25], the hybrid B3LYP [26–28] and the triple-split polarized Pople basis set 6-311G* [29–31] were used. Constrained-DFT (C-DFT) schemes were applied to localize the charge on specific molecular fragments. C-DFT calculations were performed by using the Coulomb Attenuated Method (CAM-B3LYP [32]) with the 6-311G* basis-set. All molecular geometries optimized at the DFT level showed stable equilibrium structures (no imaginary frequencies found). Geometries were also computed at the semiempirical quantum mechanical tight-binding DFT level (SQM) by using GFN2-xTB as proposed by Grimme et al. [33,34] The neutral ground state calculations were performed at the restricted DFT level while the singly charged state calculations were performed at the spin-polarized unrestricted (UDFT) level.

Bulk morphologies

The single crystalline morphologies were obtained from experimental XRD-data [21,22,35,36], while the amorphous morphologies were generated via MD simulations, where a simulated annealing procedure was employed for equilibration. Details about the force field parametrization and the MD simulations can be found in the supporting information. For all compounds, systems of 1000 molecules were initially generated by expanding as supercell the experimental unit cell.

Charge transport parameters

Marcus theory [37,38] provides the rates k_{ij} for the charge transfer between two sites *i* and *j* in the low electronic coupling regime as

$$k_{ij} = \frac{2\pi}{\hbar}\frac{J_{ij}^2}{\sqrt{4\pi\lambda k_B T}} exp\left[-\frac{(\Delta E_{ij}+\lambda)^2}{4\lambda k_B T}\right] \quad (1)$$

where J_{ij} is the electronic coupling, λ is the reorganization energy and ΔE_{ij} is the site energy difference. [37,38] The reorganization energy λ consists of an intramolecular (λ_{int}) and an external (outer) contribution (λ_o)

$$\lambda = \lambda_{int} + \lambda_o \quad (2)$$

In this work, λ_{int} was calculated at multiple levels of theory by using the adiabatic potential method. [39] λ_{int} is given by

$$\lambda_{int} = (U^{nC} - U^{nN}) + (U^{cN} - U^{cC}) \quad (3)$$

In eq. 3, *U* is the energy, the superscripted lower-case letters stand for the charge state (*n*eutral or *c*harged) while the superscripted upper-case letters stand for the geometry. For the outer reorganization energy λ_o , a constant of 50 meV was assumed. [40–42]

The electronic coupling J_{ij} between two sites *i* and *j* is given by [43]

$$J_{ij} = \langle \phi^i | \hat{H} | \phi^j \rangle \quad (4)$$

where $\phi^{i,j}$ are the highest occupied molecular orbitals (HOMOs) of the molecules taking part in the charge transfer reaction and $\hat{H}$ is the electronic Hamiltonian of the dimer. In this work, J_{ij} is calculated using the DIPRO (*DI*mer *PRO*jection) method [44] at the DFT level or the MOO (*M*olecular *O*rbital *O*verlap) approach [45] at

the semiempirical (ZINDO/S) level as implemented in the open-source package VOTCA. [44–46]

The site energy differences (ΔE_{ij}) for the crystalline and amorphous morphologies were calculated based on the static electrostatic interactions and induced dipoles, all based upon the atomic partial charges evaluated at the CHELPG level (ωB97X-D/6-311G*). The site energy E_i is given by [46,47]

$$E_i = \frac{1}{4\pi\varepsilon_0}\sum_{a_i}\sum_{b_{k,k\neq i}}\frac{(q_{a_i}^c - q_{a_i}^n)q_{b_k}^n}{\varepsilon_s r_{a_i b_k}} \qquad (5)$$

where a_i and b_k are the atomic indices running over the atoms of molecules *i* and *k*, $r_{a_i b_k}$ is the distance, q are the atomic partial charges, ε_0 is the dielectric constant of the vacuum and ε_s is the static relative dielectric constant. The sums extend over the atoms of molecule i, for which the site energy is calculated and all atoms $k \neq i$ of the surrounding molecules. To take polarization effects into account, the contribution of induced dipoles is calculated with a self-consistent approach. First, the electric field $\boldsymbol{F}_{a_i}^{(0)}$ is calculated for atom *a* in molecule *i* based on the atomic partial charges and using ε_s = 1. Subsequently, the induced dipole moments $\boldsymbol{\mu}_{a_i}^{(0)}$ can be calculated. The new induced dipoles can be iteratively computed by using $\boldsymbol{\mu}_{a_i}^{(k+1)} = \omega \boldsymbol{F}_{a_i}^{(k)}\alpha_{a_i} + (1-\omega)\boldsymbol{\mu}_{a_i}^{(k)}$ where ω is the successive over-relaxation factor and α_{a_i} is the atomic polarizability. From this, the new electric fields are obtained and the process continues until the difference between the induced dipoles is consistent with the convergence criterion of 10^{-6} Debye. A fixed set of atomic polarizabilities was used (Thole approximation), as implemented in VOTCA. [46,47]

Charge transport simulations

The charge transport simulations (hopping regime) were performed using a kinetic Monte Carlo (KMC) approach, based on the Marcus charge transfer rates calculated via eq. (1). The charge transport parameters, such as the coupling and the site energies, were computed separately for the entire system before each KMC run. The KMC simulations were performed in periodic boundary conditions for a single charge at a temperature of 300 K, using 1000 trajectories of 10^5 steps each. The diffusion coefficient (D) was obtained by a linear fit to the mean square displacements and the zero-field mobility was computed via the Einstein-Smoluchowski relation:

$$\mu = \frac{De}{k_B T} \qquad (6)$$

The KMC procedure was repeated for ten snapshots as extracted from the MD production run at a temperature of 300 K. The final hole mobilities are averaged over all KMC trajectories obtained from the ten snapshots. [48] With the charge mobility being a tensor, we refer here to μ as the average value (i.e. $\mu_{average} = \frac{1}{3}(\mu_{xx} + \mu_{yy} + \mu_{zz})$, with μ_{ii} being the *i,i*-component of the mobility tensor, *i* ∈ x, y, z). For those cases where the charge transport presents a pronounced anisotropy, single values of the tensor along specific axes are specified (vide infra, Table 3). Charge transport simulations were also performed with an applied electric field of $10^8 \frac{\mathrm{V}}{\mathrm{m}}$. The results for these last simulations are listed in the supporting information.

Software

DFT calculations were performed by combining the codes GAUSSIAN [49] and ORCA [50], C-DFT was carried out by using NWChem [51], while GFN2-xTB calculations were done with xTB [33,34]. MD simulations were executed with GROMACS, [52–56] using an in-house re-parameterized version of the OPLS-AA force field [57,58] (see supporting information for details). The evaluation of the electronic couplings were done by using the open-source code VOTCA [46] for both the crystalline and amorphous bulk morphologies. For crytalline morphologies, additionally an in-house DIPRO script interfaced with Gaussian and ORCA was also adopted. Charge transport simulations for crystalline structures were performed (and internally compared for consistency) by using two codes: an in-house code developed by Negri et al. [59–61] and the open-source code VOTCA [46]. Charge transport simulations for amorphous morphologies were done with VOTCA.

Results and discussion

1.) Bulk morphologies: crystalline vs. amorphous phases

The center-of-mass (CoM) radial distribution functions ($g_{CoM}(r)$) of the simulated amorphous and experimental single crystalline [21,22,35,36] morphologies for each compound, as reported in Figure 2, show clear differences that can be traced back to the molecular structure and the short-/long-range supramolecular packing.

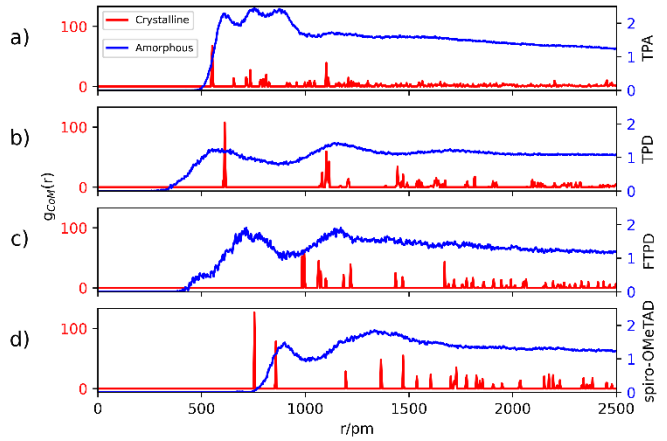

Figure 2: Center-of-mass (CoM) radial distribution functions $g_{CoM}(r)$ in the crystalline (red) and amorphous (blue) morphologies. Crystalline structures of **TPA**, **TPD**, **FTPD** and ***spiro*-OMeTAD** are taken from references [21,22,35,36], bulk amorphous structures are obtained from MD simulations (see details in computational methods and supporting information).

Generally, in the amorphous phase $g_{CoM}(r)$ is a continuous distribution characterized by broad bands reflecting different nearest-neighbours coordination shells and a lack of long-range structural order, while in the crystalline phase, as expected, $g_{CoM}(r)$ consists of narrow and well-defined peaks, according to the periodic structural order proper of crystals. Notably, the different molecular sizes and shapes of the **TPA** derivatives impact $g_{CoM}(r)$ of both crystalline and amorphous phases.

For **TPA** in the crystal phase, $g_{CoM}(r)$ shows an intense peak at 551 pm and many small peaks centered at well-defined distances. In the amorphous phase, $g_{CoM}(r)$ shows three broad bands from 600 pm to 800 pm, followed by a constant distribution at higher distances. The three bands reflect a short-range structural order, showing the formation of multiple coordination shells around each **TPA**. Such local structural order, induced by the isotropic molecular structure (sphere-like shape) of **TPA**, is however lost for large distances (r > 1000 pm).

TPD, featuring two redox-centers, is characterized by a more elongated and, therefore, anisotropic molecular structure in contrast to **TPA**. This is also reflected in the herringbone-type packing in the crystalline phase of **TPD** (See SI), leading to larger CoM distances and more defined coordination shells. In the amorphous phase, the $g_{CoM}(r)$ of **TPD** shows two very broad coordination shells, centered around the crystalline peaks at 600 pm and 1200 pm, with contributions falling off to smaller values than **TPA** (< 500 pm). This is caused by a fraction of molecules that can get very close to each other affording very short CoM distances, a feature which is enabled in the amorphous phase by the elongated and flexible structure of **TPD**.

FTPD shows an elongated structure similar to **TPD,** however it is characterised by a more rigid backbone due to the suppression of the inter-ring torsional degree of freedom via the fluorene structure. The $g_{CoM}(r)$ of the crystalline phase of **FTPD** is therefore very much different from those of **TPD** and **TPA**, showing the first coordination peak at around 1000 pm. However, similarly to **TPD**, in the amorphous case the first coordination shell of **FTPD** is computed at lower values than the crystalline phase, namely at around 750 pm, showing a broad band falling off below 500 pm, thus indicating close CoM distances between the molecules. These results suggest that molecules with elongated shapes enable short range packing in the amorphous phase, a situation that is however not always observed in the crystal phase. For **FTPD** such short range packing in the amorphous phase stems from cross-like pair configurations (see Figure S12, SI), i.e. pairs where the molecules cross along their long axes forming an X-shaped structure. Such configuration enables small CoM distances.

For crystalline ***spiro*-OMeTAD**, the coordination shells are located at higher values than **TPA**, **TPD** and **FTPD**, thus showing the very bulky nature of the molecule. In the amorphous phase, a sharp coordination shell around 800 pm, followed by a very broad band centered at 1200 pm, are observed. Only a very small fraction of the molecules gets closer (~ 650 pm) than in the crystal. Generally, the steric hindrance and the aspect ratio of the molecule prevent close contacts also in the amorphous phase, in contrast to **TPD** and **FTPD**. With respect to other **TPA**s, ***spiro*-OMeTAD** shows the highest CoM distance of the first $g_{CoM}(r)$ peak in the amorphous phase, which reflects the bulkier nature of ***spiro*-OMeTAD** as compared to the other compounds.

From the structural investigation in solid phases we can draw some partial conclusions based on the molecular structures: (i) as expected, small, sphere-like, one-redox center systems (e.g., **TPA**) show smaller CoM distances in crystalline phase than the elongated and bulkier derivatives (e.g., **TPD**, **FTPD** and ***spiro*-OMeTAD**), however (ii) elongated two-redox centers derivatives (e.g., **TPD** and **FTPD**), afford short CoM distances in the amorphous phase thanks to their structural flexibility and molecular aspect ratio. Finally, (iii) sterically demanding four-redox centers compounds (e.g., ***spiro*-OMeTAD**) present the largest CoM distances in both crystalline and amorphous phases due to their bulky nature.

2a.) Charge transport parameters: hole reorganization energy

The first charge transport parameter we computed is the internal (intramolecular) reorganization energy λ_{int}. λ_{int} was calculated at multiple levels of theory (Table 1), encompassing DFT, SQM and constrained-DFT (C-DFT), by assuming the charge partitioning

schemes as reported in Figure 3. An additional calculation of λ_{int} using the BLYP35 functional, as previously introduced by Renz et al. for the quantum-chemical characterization of mixed-valence systems, [62] can be found in Table S12 of the SI.

Table 1: Calculated (DFT, C-DFT and SQM) internal hole reorganization energies (λ_{int}, eV). Different partitioning schemes for the C-DFT calculations are labeled as c_i (i = 0-3). For the DFT calculations, the 6-311G* basis set was used. In the case of ***spiro*-OMeTAD**, due to the elevated computational costs, for C-DFT schemes c_1-c_3, the geometries optimized at the 6-31G level were used employing single-point calculations at the 6-311G* level. In the frozen dihedral approach (fda), the dihedral angles were fixed during the geometry optimizations of the charged state at their neutral ground state positions.

	TPA	**TPD**	**FTPD**	***spiro*-OMeTAD**
ωB97X-D	0.12	0.73	0.54	0.50
ωB97X-D (fda)	0.12	0.26	0.33	0.25
B3LYP	0.11	0.30	0.23	0.16
GFN2-xTB	0.07	0.09	0.12	0.08
CAM-B3LYP, c_0	0.13	0.67	0.48	0.53
CAM-B3LYP, c_1	0.10	0.10	0.31	0.24
CAM-B3LYP, c_2	-	0.60	0.57	0.46
CAM-B3LYP, c_3	-	0.20	0.32	0.30

All methods are largely consistent for **TPA**, leading to hole reorganization energy values around 0.1 eV, very much in accordance with literature data. [23] Moving to two- (**TPD** and **FTPD**) and four redox units (***spiro*-OMeTAD**) all methods yield very different results. This discrepancy can be traced back to the well-known self-interaction error (SIE), which in the case of B3LYP and GFN2-xTB leads to an artificial stabilization of the charged state. [63] When long range corrected schemes are taken into account (e.g. CAM-B3LYP, ωB97X-D) the reorganization energy raises up to 0.73 eV for **TPD**. Similar findings have been reported by Li et al. [64] and by Blaskovitz et al. [24] This result shows that an accurate description of the reorganization energy is not trivial. While the SIE can be mitigated by using a range-separated functional like ωB97X-D, Renz et al. have reported that mixed-valence systems - very similar to **TPD** - are borderline cases of the Robin-Day classification, with a charged state being on the border between delocalization and partial localization. [62] This circumstance has an additional impact on the final value of the reorganization energy. BLYP35, as introduced by Renz et al., resulted in similar reorganization energy values as B3LYP, showing the lowest for **TPA** and the highest for **TPD**. Here, we suggest an alternative approach to describe the reorganization energy by taking into account both the SIE and the partial localization problem.

To characterize the nature of the charged state, we devised multiple charge-constrain partitioning schemes at the C-DFT level, as reported in Figure 3 (for the sake of simplicity only **TPD** is shown) and recalculated the reorganization energy accordingly. The partitioning serves to characterize the extreme cases of full delocalization (c_0 and c_2) versus full localization (c_1 and c_3). The SIE is mitigated by using the range separated CAM-B3LYP functional.

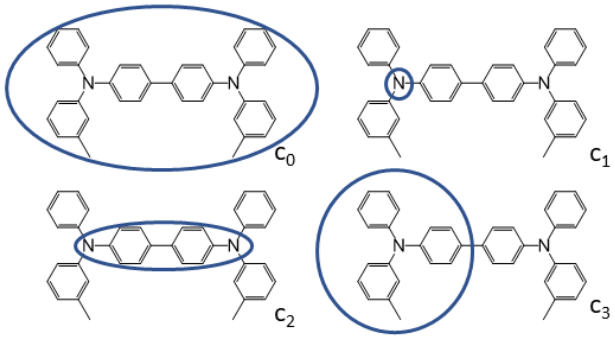

Figure 3: Charge constrain schemes for **TPD**. The circles indicate the domains where the positive charge is localized. Charge-constrain schemes for **FTPD** and ***spiro*-OMeTAD** are reported in the supporting information.

We compared the unconstrained situation (c_0, normal DFT) to different charge partitioning schemes, namely the charge confined to one nitrogen atom (c_1), to the central bridging unit (c_2), or to one **TPA**-subunit (c_3). Generally, the reorganization energies computed with C-DFT-schemes c_1 and c_3 are similar to those evaluated at the B3LYP level, while the reorganization energies computed with C-DFT-schemes c_0 and c_2 are similar to those calculated at the ωB97X-D level. In C-DFT-schemes c_0 and c_2 the charge is allowed to delocalize across the bridge and since the functional used (CAM-B3LYP) is a range-separated one, similar results as by using ωB97X-D are obtained. For the C-DFT-schemes c_1 and c_3 a lower reorganization energy is obtained than c_0 and c_2 by avoiding the charge delocalization across the whole molecular backbone. This trend shows that the delocalization of the charge across the bridge connecting the redox centers is the main factor governing the magnitude of the reorganization energies in multi-**TPA** species. Still, what remains to be answered is which kind of scenario (localized or delocalized charged state), is more realistic when modeling charge transfer processes in bulk **TPA**-based materials, which we approach by analysing the charged state geometries.

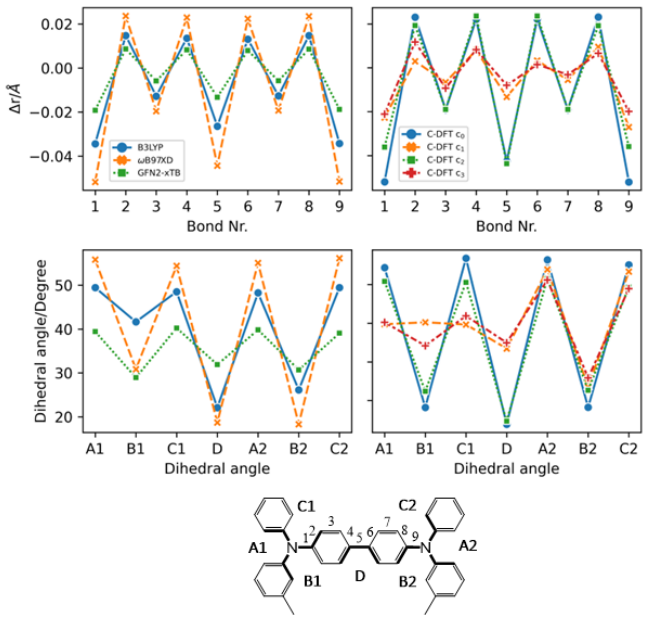

Figure 4: Geometric parameters of **TPD** in the charged state (+1) by considering different methods (DFT, C-DFT, GFN2-xTB), DFT functionals and various charge constraint (C-DFT) schemes. The two panels on the top show the bond length difference ($\Delta r = r_{charged} - r_{neutral}$) patterns by moving from the neutral to the charged state. Top left panel: DFT (B3LYP vs. ωB97X-D) versus GFN2-xTB data. Top right panel: C-DFT data with different schemes. The two panels on the bottom show the dihedral angles in the charged state. Bottom left panel: DFT (B3LYP vs. ωB97X-D) versus GFN2-xTB data. Bottom right panel: C-DFT data with different charge constraint schemes. See supporting information (Figure S4 and S6) for the geometric parameters of the other compounds.

From Figure 4 the effects of charge delocalization become clear (data for **FTPD** and ***spiro*-OMeTAD**, respectively, are reported in Figure S4 and S6 of the SI). In the unconstrained/delocalized schemes (i.e., c_0 and c_2 C-DFT, as well as normal DFT at B3LYP and ωB97X-D levels), significant changes in the bond lengths and dihedral angles occur. Most notably, the central bond (number 5) shortens significantly, and the central dihedral angle D becomes planar (quinoid-like structure). In the constrained/localized schemes (i.e. c_1, c_3), the bond length changes are much less pronounced and an asymmetric change in the dihedral angles occurs, where only the dihedral angles of the charge-bearing **TPA**-redox subunit change significantly. Thus, a large contribution to the reorganization energy can be related to the variation of the dihedral angles.

This feature was already reported by Friedrich et al. [17] Since the steric demands of the surrounding molecules in the bulk phase presumably hinders large dihedral relaxations upon charging, we recalculated the reorganization energy by fixing the dihedral angles at the values they assumed in the neutral state, similar to reports in literature. [17] Very similar reorganization energies as compared to those obtained by the C-DFT scheme c_3 values were computed (see fda approach in Table 1). Therefore, either assuming a charge localization (C-DFT) or a frozen dihedral approach leads to the same effects. Constraining the dihedral angles prevents the multi-**TPA** compounds to assume a quinoidal structure upon charging, thus corresponding to a delocalization restraint. In this work we assume for the final calculation of the charge transfer rates and mobility the intramolecular reorganization energy as obtained by C-DFT scheme c_3 for **TPD**, **FTPD** and ***spiro*-OMeTAD** and c_0 (unconstrained) for **TPA**.

Summarizing, by constraining the charge over one **TPA** redox unit (c_3 scheme) as suggested by chemical intuition, the reorganization energy smoothly increases from 0.10 eV for **TPA**, up to 0.20-0.30 eV for the two- (**TPD**, **FTPD**) and four-redox centers (***spiro*-OMeTDAD**) cases. We believe that this trend reflects the dispersion of the hole reorganization energy by moving from one to multiple **TPA** centers, also mimicking the structural constraints as induced in bulk phase by the surrounding molecules. Globally, our computational analysis shows that the hole reorganization energy in multi-redox **TPA** compounds is intrinsically linked to the degree of charge delocalization across units, and thus the variation of the central bond lengths and dihedral angles upon charging. The computed reorganization energies are however still approximate in nature, with the *true* reorganization energy lying in between the localized/frozen dihedral energies and the unconstrained calculations (e.g., using the BLYP35 functional), corresponding to a probably partially localized situation.

2b.) Charge transport parameters: site energy differences

The impact of morphological order becomes apparent when analysing the charge transport parameters, like the site energy difference distributions ΔE_{ij} (see eq. 1) as shown in Figure 5.

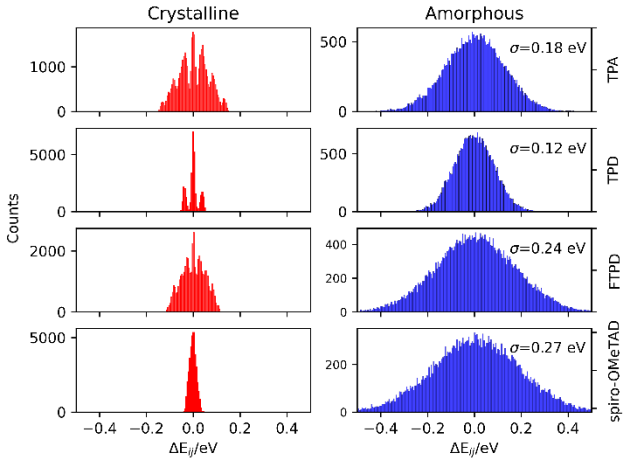

Figure 5: Histograms of the computed site energy difference distributions (ΔE_{ij}) for the experimental crystalline (left) and MD-generated amorphous (right) phases of **TPA**, **TPD**, **FTPD** and ***spiro*-OMeTAD**. For the amorphous phase the standard deviation (σ) of the site energy difference distributions is reported for each case.

As it can be generally expected, rather discrete ΔE_{ij} distributions are found for single crystalline phases, while the amorphous phases show much wider, Gaussian-like shapes due to the statistical

distribution of conformers. The nonequivalent molecular sites of the crystalline phases are reflected in the peaks of the histograms, with each peak being slightly broadened due to the finite numerical accuracy in the calculation of the site energies. The electrostatic disorder, quantified as the standard deviation σ of the site energy difference distributions in the amorphous phase, is of a similar magnitude as the reorganization energies for each compound. Such feature leads to the static disorder being the dominating parameter for hopping transport in the amorphous phase. On the other hand, the site-energy difference distributions in the crystalline phases are narrower, causing the reorganization energy to be the dominant parameter for the hopping transport in crystals. Comparable values for the static disorder have been reported by Friedrich et al. [17], Lin et al. [20] and Mondal et al. [19] Comparing the σ-values, molecules characterized by an increased structural complexity like **FTPD** and ***spiro*-OMeTAD** show increased electrostatic disorder effects in the amorphous phase when compared to **TPA** and **TPD**.

2c.) Charge transport parameters: electronic couplings

The electronic coupling distributions (Figure 6) as computed for both crystalline and amorphous morphologies, show similar characteristics as the site energy difference distributions, being continuous in the amorphous phase and discrete in the crystalline phase. Generally, low values are obtained for the electronic coupling (largest J_{ij} is around 20 meV), clearly supporting the observation of a disorder-controlled nature of the charge transport.

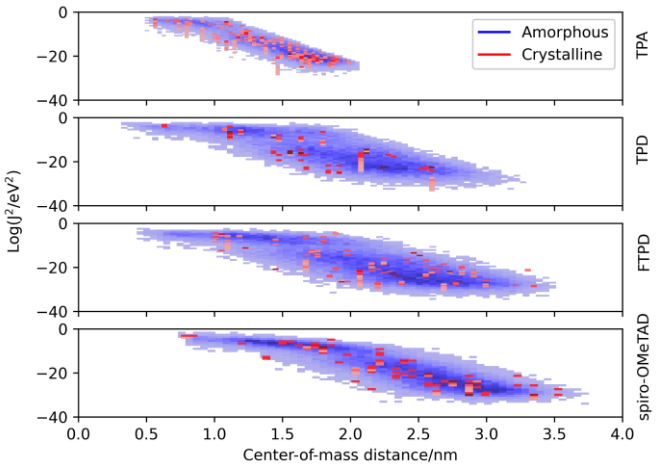

Figure 6: Coupling integral distributions ($Log(J_{ij}^2/eV^2)$) as calculated with the MOO approach (ZINDO/S) versus center-of-mass (CoM) distance in experimental crystalline (red) and MD generated amorphous (blue) phases.

Comparing the molecular classes, we notice that the coupling distribution in the **TPA** crystal is much more narrow than **TPD**, **FTPD** and ***spiro*-OMeTAD** crystals, reflecting the smaller size and sphere-like shape (isotropy) of the molecule. For **TPD**, **FTPD** and ***spiro*-OMeTAD**, broader distributions are obtained, and even at large CoM distances (> 2 nm) nonzero electronic coupling is found due to the elongated or bulky shape of the molecules. In the amorphous phase, we can observe that there are two trends for the couplings, a horizontal dispersion (from roughly 0.5 to 1.5 nm) and a linear one (from 2.0 to 3.5 pm). In the first range, the couplings are almost independent from the CoM distances, indicating the interplanar distance as the determining factor for the magnitude of the coupling, while at larger CoM distances, the coupling drops approximately linearly, indicating a crossing point at which the CoM distance becomes the dominating factor ruling the strength of the electronic coupling. Considering the logarithmic scale, this linear decrease corresponds to an exponential decrease in a linear scale.

Analysis of the electronic couplings based on the experimental crystal structures

To gain an in-depth understanding about the influence of solid-state packing and molecular orientations on the electronic coupling, the crystal structures of **TPA**, **TPD**, **FTPD** and ***spiro*-OMeTAD** were analysed by calculating the electronic coupling using the DIPRO approach (ωB97X-D/6-311G*) for each unique molecular site and its neighbours, applying a cutoff of 1.5 nm. A detailed listing of the results and the geometric parameters can be found in the SI (Tables S2-S9). For **TPA**, **TPD** and **FTPD** three non-equivalent pairs (couplings) can be isolated, named A, B and C in Table 2. For ***spiro*-OMeTAD** only two pairs are identified (A and B).

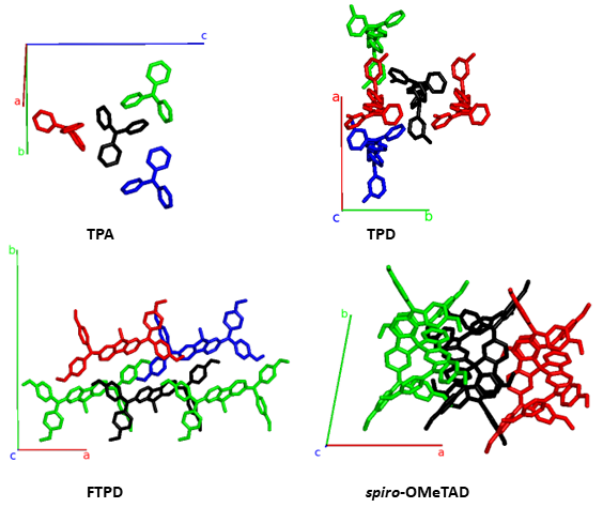

Figure 7: Structures featuring the largest electronic coupling (see main text) from the **TPA**- **TPD**-, **FTPD**- and ***spiro*-OMeTAD** crystal unit cells, also reporting the crystallographic axes. The central molecule is shown in black. The pair formed by the black and red molecules is, for each compound, the one with the highest electronic coupling, followed by the black-green and black-blue pairs, respectively (see Table 2).

Table 2: Electronic couplings (J_{ij}, meV) for the pairs shown in Figure 7. Pair A refers to the pair formed from the black and red monomers, pair B to the pair formed from the black and green monomers and pair C to the pair formed from the black and blue monomers. ***spiro*-OMeTAD** shows only A and B type pairs.

	TPA	TPD	FTPD	*spiro*-OMeTAD
A (black-red)	50	36	9.8	39
B (black-green)	40	11	9.3	15
C (black-blue)	36	8	9	

From Figure 7 and Table 2 we can observe that **TPA** shows the highest electronic couplings amongst the triphenylamine series. Furthermore, the highest **TPA** coupling (50 meV) results from an interdigitation of the amine moieties, see pair A (black-red pair). For **TPA**, all couplings are of the same order of magnitude, thus, an isotropic transport of the charges within the crystal is to be expected. For **TPD** a similar interdigitation motif as for **TPA** is found (pair A), resulting in a high electronic coupling (36 meV). However, in contrast to **TPA**, for **TPD** the other couplings (pairs B and C) are smaller in magnitude than pair A. Because pair A of **TPD** is prevalently aligned with the crystallographic axis *b*, charge transport is expected to occur preferably along this direction in an anisotropic way in the crystal. For the case of **FTPD**, lower couplings (~10 meV) are observed when compared to the other triphenylamine compounds. This can be due to the shifted orientation of the monomers in the crystal packing, which prevents close contact between the molecular backbones (as reported in the $g_{CoM}(r)$, Figure 2) and the interdigitation of the triphenylamine moieties. All **FTPD** couplings are very similar in magnitude, in accordance with Ref. [21], making an isotropic-like charge transport in the crystal probable. Finally, for ***spiro*-OMeTAD**, one can observe that pair A is more intertwined than the others, leading to higher electronic coupling (39 meV), in accordance with Ref. [21], possibly resulting in an anisotropic charge diffusion as for the case of **TPD** crystal.

Kinetic Monte-Carlo charge transport simulations and zero-field (Brownian) hole mobilities

The computed KMC charge percolation pathways for single crystals, as reported in Figure 8, show the expected characteristics as anticipated from the analysis of the electronic couplings. While for **TPA**, due to its molecular shape (sphere-like) and solid state packing, isotropic charge transport is found, other compounds show either marked anisotropic charge diffusion (**TPD** and ***spiro*-OMeTAD**) or weak anisotropic charge percolation (**FTPD**) due to different molecular aspect ratio, bridge flexibility, steric hindrance and packing motifs. In **TPD**, the *b* direction is clearly favoured over the *a* and *c* axes (Figure 7). Such preferred direction is readily explained by the orientation of the main charge transport pairs (i.e., those showing the highest J_{ij}) along the *b* axis (Figure 7 and Table 2), as favoured by the elongated molecular shape and interdigitation of the nearest neighbour **TPA** units. In the charge mobility simulations of single crystal **FTPD**, a weak anisotropy of the charge transport along *a* axis is observed, due to the similar (small) magnitude of the electronic coupling in all charge transport pairs (~ 9 meV, Table 2). In the charge hopping pathways of ***spiro*-OMeTAD**, the charge transport takes place mainly along the *a* axis due to the high coupling (39 meV) on the basis of the π- π stacking along this direction (Figure 7).

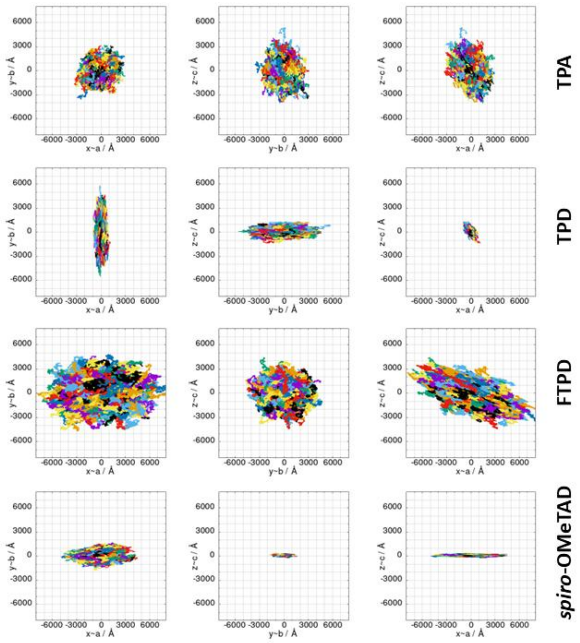

Figure 8: KMC charge hopping trajectories for all **TPA**s here investigated, evaluated for the experimental single crystal structures, shown from different planes. The colours used in the plots only serve to discern the superimposed trajectories.

Table 3 collects the computed zero-field (Brownian) KMC hole mobilities (that is, $\mu_{average} = \frac{1}{3}(\mu_{xx} + \mu_{yy} + \mu_{zz})$, with μ_{ii} being the *i,i*-component of the mobility tensor, *i* ∈ x, y, z) for all species in their crystalline and amorphous phases. In Table 3 are also shown the experimental data available from literature. A one-to-one comparison between the computed single crystal/amorphous charge mobility and the experimental single crystal/amorphous-films hole mobility was sometimes not possible to do. For instance, for **TPA** only the experimental single crystal hole mobility was found, while no data is available for amorphous films. The only case we could find both single crystal and amorphous measured hole mobility is ***spiro*-OMeTAD**. In Supporting Information are reported the computed mobilities in the presence of an electric field (Table S10). Furthermore, we report also the μ_{xx}, μ_{yy}, μ_{zz} components in order to highlight the isotropy vs. anisotropy of the charge transport in single crystals.

By moving from the crystalline to the amorphous phase a drop of various orders of magnitude of the charge mobility occurs, as expected due to the impact of morphological (Figure 2) and energetic (Figure 5) disorder. This phenomenon is, however, more drastic in the case of **FTPD** and ***spiro*-OMeTAD**, due to the higher σ value of the site energy difference distributions in the amorphous phase (Figure 5). In the crystalline phase, the computed hole mobilities are generally comparable to each other (~ 10^{-2} $cm^2V^{-1}s^{-1}$), with the only exception of **FTPD**, which has a lower average mobility, probably due to the rather low values of the electronic couplings (around 9 meV), as compared to the other triphenylamines. For those cases in which the experimental single crystal hole mobility is available in literature, that are **TPA** and ***spiro*-OMeTAD** (Table 3), the computed hole mobilities of single crystals are in very good agreement with the measured one. For **TPD** we could not find experimental data referring to single crystals, while for **FTPD** the experimental values refer to semi-crystalline thin films. Clearly, our simulations on a single crystal do not take into account the presence of defects (e.g., vacancies, dislocations), impurities or grain boundaries, thus overestimating the charge mobility. We note that one can not trivially infer the magnitude of the charge mobility from the size of the area covered by the superimposed trajectories (Figure 8) alone when comparing different compounds, since the time it took to complete the trajectories is not visible in the plots and the same number of KMC steps is performed in all cases. The anisotropy of the mobility tensors however can be clearly observed.

Table 3: Computed Brownian hole mobilities (μ, $[\frac{cm^2}{Vs}]$) for single crystal and amorphous phases. Computed Brownian hole mobilites along the x, y and z axes (μ_{xx}, μ_{yy}, μ_{zz}) for each single crystal. Experimental mobilities can refer to single crystal (**TPA**, ***spiro*-OMeTAD**), amorphous (**TPD**, ***spiro*-OMeTAD**) or semicrystalline thin films (**FTPD**), as taken from literature.

	TPA	**TPD**	**FTPD**	***spiro*-OMeTAD**
computed *(single crystal)*				
$\mu_{average}$	$2.5 \cdot 10^{-2}$	$5.9 \cdot 10^{-2}$	$1.0 \cdot 10^{-3}$	$1.6 \cdot 10^{-2}$
μ_{xx}	$2.3 \cdot 10^{-2}$	$7.1 \cdot 10^{-3}$	$1.8 \cdot 10^{-3}$	$4.3 \cdot 10^{-2}$
μ_{yy}	$2.2 \cdot 10^{-2}$	$1.6 \cdot 10^{-1}$	$8.6 \cdot 10^{-4}$	$5.3 \cdot 10^{-3}$
μ_{zz}	$3.1 \cdot 10^{-2}$	$1.1 \cdot 10^{-2}$	$4.5 \cdot 10^{-4}$	$3.4 \cdot 10^{-4}$
computed *(amorphous)*				
$\mu_{average}$	$8.3 \cdot 10^{-4}$	$5.9 \cdot 10^{-4}$	$3.1 \cdot 10^{-6}$	$2.3 \cdot 10^{-6}$
Experimental data from literature	$2 \cdot 10^{-2}$ [65] *(single crystal)*	$1 \cdot 10^{-3}$ [1] *(amorphous thin film)*	$4.3 \cdot 10^{-4}$ [21] *(semicrystalline thin film)*	$1.30 \cdot 10^{-3}$ [22] *(single crystal)* $1.69 \cdot 10^{-6}$ [22] *(amorphous thin film)*

Comparing the results from the KMC charge transport simulations in the crystalline and amorphous morphologies (see also SI, Figure S11), besides the drop of the hole mobility from two to four orders of magnitude (which is expected for small molecules), one can also observe the loss of directional anisotropy, especially for **TPD** and ***spiro*-OMeTAD**, which show clear preferential charge percolation directions in single crystals. Interestingly, for these anisotropic cases (**TPD** and ***spiro*-OMeTAD**), the highest computed hole mobility (μ_{yy} = 1.6x10^{-1} $cm^2V^{-1}s^{-1}$ for **TPD** and μ_{xx} = 4.3x10^{-2} $cm^2V^{-1}s^{-1}$ for ***spiro*-OMeTAD**) can be one or two orders of magnitude larger than the other components of the mobility tensor. Such knowledge can pave the way for exploiting morphologically controlled experimental techniques to grow the **TPA**s crystals along with particular directions, in order to enhance the hole mobility.

In the amorphous bulk morphology all triphenylamines show isotropic Brownian charge diffusion. This feature is related to the loss of structural order passing from the crystal to the amorphous phase, as suggested by the radial distribution function analysis (Figure 2). **TPA** and **TPD** show the highest computed hole mobilities (8.3 and 5.9·10^{-4} $cm^2V^{-1}s^{-1}$) in the amorphous phase, two order of magnitudes higher than **FTPD** and ***spiro*-OMeTAD** (~10^{-6} $cm^2V^{-1}s^{-1}$). Such differences originate from the site energy disorder (Figure 4), which is lower for **TPA** and **TPD** (σ = 0.18 and 0.12 meV, respectively) with respect to **FTPD** and ***spiro*-OMeTAD** (σ = 0.24 and 0.27 meV, respectively). The broad site energy difference distributions in the amorphous phase of each species leads to charge trapping and low charge transfer rates, thus impacting the final zero-field charge mobility. A good agreement is achieved between the computed charge mobility for the amorphous phase with respect to the available experimental data, as for the cases of **TPD** and ***spiro*-MeOTAD**.

Conclusion

We have presented an in-depth study about the interplay between the structural complexity, the supramolecular packing in the crystalline and amorphous condensed phases, and the charge transport parameters of four triphenylamine derivatives. The influence of the molecular architecture can be observed in the radial distribution function characterising the CoM distances at short- and long-range, in both the crystalline and amorphous phases. In the crystal phase, small, sphere-like compounds like **TPA** can get very close to each other, resulting in packed structures, while elongated two-redox center (**TPD**, **FTPD**) or sterically demanding four-redox center (***spiro*-OMeTAD**) compounds show very large CoM distances. In the amorphous phase, however, due to the favourable aspect ratio or backbone flexibility, the elongated two-redox centers derivatives can afford shorter CoM distances than **TPA** and ***spiro*-OMeTAD**. Such different structural order impacts the bulk charge mobility.

From the calculation of the charge transport parameters, we firstly remarked the dependence of the intramolecular reorganization energy on the degree of charge delocalization in multi-redox-center **TPA** species. Such charge delocalization is influenced by the flexibility of the molecular structure, namely the bridge connecting the redox centers. We found that reasonable reorganization energies can be computed by adopting a charge partitioning

scheme (via C-DFT), which localizes the charge on single redox **TPA** centers. This method provides values of the internal reorganization energy very close to those obtained by the well-consolidated frozen dihedral angle approach, where torsional angles are fixed upon charging, thus avoiding the twisting which is reasonably hindered in the bulk phase.

The narrow site-energy distributions in the crystalline phase as computed for all **TPA**s leads to a reorganization energy controlled hopping transport regime in single crystals. In the amorphous phase, however, the charge transport is instead dominated by the static energetic disorder. Indeed, the standard deviation of the site energy difference distributions of amorphous morphologies is larger than for crystals. In particular, the structurally complex compounds like **FTPD** and ***spiro*-OMeTAD** show higher energetic disorder than **TPA** and **TPD**, thus leading to very low (10^{-6} $cm^2V^{-1}s^{-1}$) values for the charge mobility in the amorphous phase. A detailed analysis of the crystal structures of **TPA**s with regard to molecular packing and electronic coupling distribution revealed the origin of the charge transport (an)isotropy in the single crystalline phases. In particular, elongated **TPD** or bulky ***spiro*-OMeTAD** show preferential charge diffusion along specific crystal axes, leading to strong anisotropy in the hole transport. Our work shows that in crystalline phases the average mobility is very similar for all compounds, however the charge transport anisotropy leads to charge mobility differences for some directions of multiple orders of magnitude for some species, like **TPD** and ***spiro*-OMeTAD**. Such characteristic can be potentially exploited to growth crystalline films along particular crystallographic directions, thus achieving the highest charge mobility for that compound. Generally, the computed hole mobilities are in very good agreement with the available experimental data (either measured on single crystal/semi-crysatlline films, or amorphous films), corroborating our computational approach.

Author contributions

R. H. and D. F. performed the calculations and the computational analyses. R. H., D. F., K. M. and F. N. conceptualized the work. All authors contributed to rationalize the data and write the manuscript.

Conflicts of interest

There are no conflicts of interest to declare.

Acknowledgements

D.F. acknowledges the Deutsche Forschungsgemeinschaft (DFG) for the grant (FA 1502/1-1, years 2018-2021), the Regional Computing Centre (RRZK) of University of Cologne for providing computing time and resources on the HPC RRZK CHEOPS, and partial funding from the National Recovery and Resilience Plan (NRRP), Mission 04 Component 2, Investment 1.5 – NextGenerationEU, Call for tender n. 3277 dated 30/12/2021, Award Number: 0001052 dated 23/06/2022. K. M., D. F. and R. H. acknowledge the excellence initiative of the University of Cologne, "Quantum Matter and Materials" (QM2), and the DFG Research Training Group 2591 "Template-designed Organic Electronics (TIDE)" for supporting their research.

Notes and references

1 M. Stolka, J. F. Yanus and D. M. Pai, *J. Phys. Chem.*, 1984, **88**, 4707–4714.

2 P. Cias, C. Slugovc and G. Gescheidt, *J. Phys. Chem. A*, 2011, **115**, 14519–14525.

3 C. Adachi, K. Nagai and N. Tamoto, *Appl. Phys. Lett.*, 1995, **66**, 2679–2681.

4 Y. Shirota, *J. Mater. Chem.*, 2005, **15**, 75–93.

5 J. K. Feng, Y. L. Cao, X. P. Ai and H. X. Yang, *J. Power Sources*, 2008, **177**, 199–204.

6 H. Tanaka, S. Tokito, Y. Taga and A. Okada, *Chem. Commun.*, 1996, **1**, 2175.

7 S. Tokito, H. Tanaka, K. Noda, A. Okada and Y. Taga, *Appl. Phys. Lett.*, 1997, **70**, 1929–1931.

8 P. Agarwala and D. Kabra, *J. Mater. Chem. A*, 2017, **5**, 1348–1373.

9 P. Blanchard, C. Malacrida, C. Cabanetos, J. Roncali and S. Ludwigs, *Polym. Int.*, 2019, **68**, 589–606.

10 Y. Tao, Q. Wang, C. Yang, C. Zhong, J. Qin and D. Ma, *Adv. Funct. Mater.*, 2010, **20**, 2923–2929.

11 A. Leliège, P. Blanchard, T. Rousseau and J. Roncali, *Org. Lett.*, 2011, **13**, 3098–3101.

12 H. Choi, J. W. Cho, M.-S. Kang and J. Ko, *Chem. Commun.*, 2015, **51**, 9305–9308.

13 N. Goujon, N. Casado, N. Patil, R. Marcilla and D. Mecerreyes, *Prog. Polym. Sci.*, 2021, **122**, 101449.

14 L. Fan, Q. Liu, Z. Xu and B. Lu, *ACS Energy Lett.*, 2017, **2**, 1614–1620.

15 S. Feser and K. Meerholz, *Chem. Mater.*, 2011, **23**, 5001–5005.

16 P. Zacharias, M. C. Gather, M. Rojahn, O. Nuyken and K. Meerholz, *Angew. Chem., Int. Ed. Engl.*, 2007, **46**, 4388–4392.

17 P. Friederich, V. Meded, A. Poschlad, T. Neumann, V. Rodin, V. Stehr, F. Symalla, D. Danilov, G. Lüdemann, R. F. Fink, I. Kondov, F. von Wrochem and W. Wenzel, *Adv. Funct. Mater.*, 2016, **26**, 5757–5763.

18 K.-H. Lin, L. Paterson, F. May and D. Andrienko, *NPJ Comput. Mater.*, 2021, **7**, 1–7.

19 A. Mondal, L. Paterson, J. Cho, K.-H. Lin, B. van der Zee, G.-J. A. H. Wetzelaer, A. Stankevych, A. Vakhnin, J.-J. Kim, A. Kadashchuk, P. W. M. Blom, F. May and D. Andrienko, *Chem. Phys. Rev.*, 2021, **2**, 31304.

20 K.-H. Lin, A. Prlj, L. Yao, N. Drigo, H.-H. Cho, M. K. Nazeeruddin, K. Sivula and C. Corminboeuf, *Chem. Mater.*, 2019, **31**, 6605–6614.

21 L. Fang, A. Zheng, M. Ren, X. Xie and P. Wang, *ACS Appl. Mater. Interfaces*, 2019, **11**, 39001–39009.

22 D. Shi, X. Qin, Y. Li, Y. He, C. Zhong, J. Pan, H. Dong, W. Xu, T. Li, W. Hu, J.-L. Brédas and O. M. Bakr, *Sci. Adv.*, 2016, **2**, e1501491.

23 B. C. Lin, C. P. Cheng and Z. P. M. Lao, *J. Phys. Chem. A*, 2003, **107**, 5241–5251.

24 J. T. Blaskovits, K.-H. Lin, R. Fabregat, I. Swiderska, H. Wu and C. Corminboeuf, *J. Phys. Chem. C*, 2021, **125**, 17355–17362.

25 J.-D. Chai and M. Head-Gordon, *Phys. Chem. Chem. Phys.*, 2008, **10**, 6615–6620.

26 AD Becke, *J. Chem. Phys.*, 1993, **98**, 5648–5652.

27 Lee, Yang and Parr, *Phys. Rev. B*, 1988, **37**, 785–789.

28 S. H. Vosko, L. Wilk and M. Nusair, *Can. J. Phys.*, 1980, **58**, 1200–1211.

29 R. Krishnan, J. S. Binkley, R. Seeger and J. A. Pople, *J. Chem. Phys.*, 1980, **72**, 650–654.

30 B. P. Pritchard, D. Altarawy, B. Didier, T. D. Gibson and T. L. Windus, *J. Chem. Inf. Model.*, 2019, **59**, 4814–4820.

31 T. Clark, J. Chandrasekhar, G. W. Spitznagel and P. V. R. Schleyer, *J. Comput. Chem.*, 1983, **4**, 294–301.

32 T. Yanai, D. P. Tew and N. C. Handy, *Chem. Phys. Lett.*, 2004, **393**, 51–57.

33 C. Bannwarth, E. Caldeweyher, S. Ehlert, A. Hansen, P. Pracht, J. Seibert, S. Spicher and S. Grimme, *WIREs comput. mol. sci.*, 2021, **11**. DOI: 10.1002/wcms.1493.

34 C. Bannwarth, S. Ehlert and S. Grimme, *J. Chem. Theory Comput.*, 2019, **15**, 1652–1671.

35 K. Ramachandran, A. Raja, N. Lingamurthy, M. S. Pandian, P. Ramasamy and S. Venugopal Rao, *Chem. Phys. Lett.*, 2020, **742**, 137128.

36 Z. Zhang, E. Burkholder and J. Zubieta, *Acta Cryst. C*, 2004, **60**, o452-4.

37 R. A. Marcus, *Angew. Chem., Int. Ed. Engl.*, 1993, **32**, 1111–1121.

38 R. A. Marcus and N. Sutin, *Biochim. Biophys. Acta - Bioenerg.*, 1985, **811**, 265–322.

39 S. F. Nelsen, S. C. Blackstock and Y. Kim, *J. Am. Chem. Soc.*, 1987, **109**, 677–682.

40 S. Di Motta, E. Di Donato, F. Negri, G. Orlandi, D. Fazzi and C. Castiglioni, *J. Am. Chem. Soc.*, 2009, **131**, 6591–6598.

41 D. P. McMahon and A. Troisi, *J. Phys. Chem. Lett.*, 2010, **1**, 941–946.

42 J. E. Norton and J.-L. Brédas, *J. Am. Chem. Soc.*, 2008, **130**, 12377–12384.

43 E. F. Valeev, V. Coropceanu, D. A. Da Silva Filho, S. Salman and J.-L. Brédas, *J. Am. Chem. Soc.*, 2006, **128**, 9882–9886.

44 B. Baumeier, J. Kirkpatrick and D. Andrienko, *Phys. Chem. Chem. Phys.*, 2010, **12**, 11103–11113.

45 J. Kirkpatrick, *Int. J. Quantum Chem.*, 2008, **108**, 51–56.

46 V. Rühle, A. Lukyanov, F. May, M. Schrader, T. Vehoff, J. Kirkpatrick, B. Baumeier and D. Andrienko, *J. Chem. Theory Comput.*, 2011, **7**, 3335–3345.

47 J. Kirkpatrick, V. Marcon, K. Kremer, J. Nelson and D. Andrienko, *J. Chem. Phys.*, 2008, **129**, 94506.

48 I. Yavuz, B. N. Martin, J. Park and K. N. Houk, *J. Am. Chem. Soc.*, 2015, **137**, 2856–2866.

49 M. J. Frisch, G. W. Trucks, H. B. Schlegel, G. E. Scuseria, M. A. Robb, J. R. Cheeseman, G. Scalmani, V. Barone, G. A. Petersson, H. Nakatsuji, X. Li, M. Caricato, A. V. Marenich, J. Bloino, B. G. Janesko, R. Gomperts, B. Mennucci, H. P. Hratchian, J. V. Ortiz, A. F. Izmaylov, J. L. Sonnenberg, D. Williams-Young, F. Ding, F. Lipparini, F. Egidi, J. Goings, B. Peng, A. Petrone, T. Henderson, D. Ranasinghe, V. G. Zakrzewski, J. Gao, N. Rega, G. Zheng, W. Liang, M. Hada, M. Ehara, K. Toyota, R. Fukuda, J. Hasegawa, M. Ishida, T. Nakajima, Y. Honda, O. Kitao, H. Nakai, T. Vreven, K. Throssell, J. A. Montgomery, Jr., J. E. Peralta, F. Ogliaro, M. J. Bearpark, J. J. Heyd, E. N. Brothers, K. N. Kudin, V. N. Staroverov, T. A. Keith, R. Kobayashi, J. Normand, K. Raghavachari, A. P. Rendell, J. C. Burant, S. S. Iyengar, J. Tomasi, M. Cossi, J. M. Millam, M. Klene, C. Adamo, R. Cammi, J. W. Ochterski, R. L. Martin, K. Morokuma, O. Farkas, J. B. Foresman, and D. J. Fox, Gaussian, Inc., Wallingford CT, 2016.

50 F. Neese, F. Wennmohs, U. Becker and C. Riplinger, *J. Chem. Phys.*, 2020, **152**, 224108.

51 E. Aprà, E. J. Bylaska, W. A. de Jong, N. Govind, K. Kowalski, T. P. Straatsma, M. Valiev, H. J. J. van Dam, Y. Alexeev, J. Anchell, V. Anisimov, F. W. Aquino, R. Atta-Fynn, J. Autschbach, N. P. Bauman, J. C. Becca, D. E. Bernholdt, K. Bhaskaran-Nair, S. Bogatko, P. Borowski, J. Boschen, J. Brabec, A. Bruner, E. Cauët, Y. Chen, G. N. Chuev, C. J. Cramer, J. Daily, M. J. O. Deegan, T. H. Dunning, M. Dupuis, K. G. Dyall, G. I. Fann, S. A. Fischer, A. Fonari, H. Früchtl, L. Gagliardi, J. Garza, N. Gawande, S. Ghosh, K. Glaesemann, A. W. Götz, J. Hammond, V. Helms, E. D. Hermes, K. Hirao, S. Hirata, M. Jacquelin, L. Jensen, B. G. Johnson, H. Jónsson, R. A. Kendall, M. Klemm, R. Kobayashi, V. Konkov, S. Krishnamoorthy, M. Krishnan, Z. Lin, R. D. Lins, R. J. Littlefield, A. J. Logsdail, K. Lopata, W. Ma, A. V. Marenich, J. Del Martin Campo, D. Mejia-Rodriguez, J. E. Moore, J. M. Mullin, T. Nakajima, D. R. Nascimento, J. A. Nichols, P. J. Nichols, J. Nieplocha, A. Otero-de-la-Roza, B. Palmer, A. Panyala, T. Pirojsirikul, B. Peng, R. Peverati, J. Pittner, L. Pollack, R. M. Richard, P. Sadayappan, G. C. Schatz, W. A. Shelton, D. W. Silverstein, D. M. A. Smith, T. A. Soares, D. Song, M. Swart, H. L. Taylor, G. S. Thomas, V. Tipparaju, D. G. Truhlar, K. Tsemekhman, T. van Voorhis, Á. Vázquez-Mayagoitia, P. Verma, O. Villa, A. Vishnu, K. D. Vogiatzis, D. Wang, J. H. Weare, M. J. Williamson, T. L. Windus, K. Woliński, A. T. Wong, Q. Wu, C. Yang, Q. Yu, M. Zacharias, Z. Zhang, Y. Zhao and R. J. Harrison, *J. Chem. Phys.*, 2020, **152**, 184102.

52 H. Berendsen, D. van der Spoel and R. van Drunen, *Comput. Phys. Commun.*, 1995, **91**, 43–56.

53 B. Hess, C. Kutzner, D. van der Spoel and E. Lindahl, *J. Chem. Theory Comput.*, 2008, **4**, 435–447.

54 E. Lindahl, B. Hess and D. van der Spoel, *J. Mol. Model.*, 2001, **7**, 306–317.

55 S. Pronk, S. Páll, R. Schulz, P. Larsson, P. Bjelkmar, R. Apostolov, M. R. Shirts, J. C. Smith, P. M. Kasson, D. van der Spoel, B. Hess and E. Lindahl, *Bioinformatics*, 2013, **29**, 845–854.

56 D. van der Spoel, E. Lindahl, B. Hess, G. Groenhof, A. E. Mark and H. J. C. Berendsen, *J. Comput. Chem.*, 2005, **26**, 1701–1718.

57 W. L. Jorgensen, D. S. Maxwell and J. Tirado-Rives, *J. Am. Chem. Soc.*, 1996, **118**, 11225–11236.

58 G. A. Kaminski, R. A. Friesner, J. Tirado-Rives and W. L. Jorgensen, *J. Phys. Chem. B*, 2001, **105**, 6474–6487.

59 E. Di Donato, R. P. Fornari, S. Di Motta, Y. Li, Z. Wang and F. Negri, *J. Phys. Chem. B*, 2010, **114**, 5327–5334.

60 S. Di Motta, M. Siracusa and F. Negri, *J. Phys. Chem. C*, 2011, **115**, 20754–20764.

61 N. Gildemeister, G. Ricci, L. Böhner, J. M. Neudörfl, D. Hertel, F. Würthner, F. Negri, K. Meerholz and D. Fazzi, *J. Mater. Chem. C*, 2021, **9**, 10851–10864.

62 M. Renz, K. Theilacker, C. Lambert and M. Kaupp, *J. Am. Chem. Soc.*, 2009, **131**, 16292–16302.

63 M. Lundberg and P. E. M. Siegbahn, *J. Chem. Phys.*, 2005, **122**, 224103.

64 Y. Li, H. Li, C. Zhong, G. Sini and J.-L. Brédas, *NPJ Flex. Electron.*, 2017, **1**, 1–8.

65 D. C. Hoesterey and G. M. Letson, *J. Chem. Phys.*, 1964, **41**, 675–679.